Large angular scale fluctuations of near-infrared extragalactic background light based on the IRTS observations

Min Gyu Kim,[1,*] **Toshio Matsumoto,**[2] **Hyung Mok Lee,**[1,3]
Woong-Seob Jeong,[3,4] **Kohji Tsumura,**[5] **Hyunjong Seo,**[3]
and Masahiro Tanaka[6]

[1]Department of Physics and Astronomy, Seoul National University, Seoul 08826, Korea
[2]Department of Space Astronomy and Astrophysics, Institute of Space and Astronautical Science (ISAS), Japan Aerospace Exploration Agency (JAXA), 3-1-1 Yoshinodai, Chuo-ku, Sagamihara, Kanagawa 252-5210, Japan
[3]Korea Astronomy and Space Science Institute (KASI), 776 Daedeok-daero, Yuseong-gu, Daejeon 34055, Korea
[4]University of Science and Technology, Korea (UST), 217 Gajeong-ro, Yuseong-gu, Daejeon 34113, Korea
[5]Department of Natural Science, Faculty of Knowledge Engineering, Tokyo City University, 1-28-1 Tamazutsumi, Setagaya, Tokyo, 158-8557, Japan
[6]Center for Computational Sciences, University of Tsukuba, 1-1-1 Tennodai, Tsukuba, Ibaraki 305-8577, Japan

*E-mail: mgkim@astro.snu.ac.kr

Abstract

We measure the spatial fluctuations of the Near-Infrared Extragalactic Background Light (NIREBL) from $2°$ to $20°$ in angular scale at the 1.6 and 2.2 μm using data obtained with Near-Infrared Spectrometer (NIRS) on board the Infrared Telescope in Space (IRTS). The brightness of the NIREBL is estimated by subtracting foreground components such as zodiacal light, diffuse Galactic light, and integrated star light from the observed sky. The foreground components are estimated using well-established models and archive data. The NIREBL fluctuations for the 1.6 and 2.2 μm connect well toward the sub-degree scale measurements from previous studies. Overall, the fluctuations show a wide bump with a center at around $1°$ and the power decreases toward larger angular scales with nearly a single power-law spectrum (i.e., $F[\sqrt{l(l+1)C_l/2\pi}] \sim \theta^{-1}$), indicating that the large-scale power is dominated by the random spatial distribution of the sources. After examining several known sources, contributors such as normal galaxies, high-redshift objects, intrahalo light, and far-IR cosmic background, we conclude that the excess fluctuation at around the $1°$ scale cannot be explained by any of them.

Key words: cosmic background radiation — cosmology: observations — infrared: diffuse background

1 Introduction

The near-infrared extragalactic background light (NIREBL) is the integrated light of the entire cosmic history in the near-infrared. Thus, the origin of the NIREBL is essential to probe the formation and evolution of galaxies from birth to the present Universe. Since current technology limits us from resolving diffuse, faint, and distant objects that contribute to the NIREBL brightness, we should rely on measurements of spatial fluctuations and absolute brightness to understand the nature of the NIREBL. The absolute brightness measures the background intensity, and the spatial fluctuation measures the clustering properties of the emitting sources.

The first reliable measurement of the absolute brightness conducted at 1.25, 2.2, 3.5, and 4.9 μm with the Diffuse InfraRed Background Experiment (DIRBE) on the Cosmic Background Explorer (COBE) although it experienced difficulties in subtracting the contribution from Galactic stars due to a large confusion limit (Gorjian et al. 2000; Wright & Reese 2000; Cambrésy et al. 2001; Levenson et al. 2007; Sano et al. 2015, 2016). They found 2 to 8 times larger brightness than the integrated light of galaxies (ILG). Thanks to the smaller beam size and low-resolution spectrograph, the Infrared Telescope in Space (IRTS) confirmed the NIREBL excess by observing the isotropic background spectrum at short wavelengths (1.4–4 μm) with better precision (Matsumoto et al. 2005, 2015). With better point-source subtractions, AKARI also succeeded to confirm the excess NIREBL spectrum at 2–5 μm (Tsumura et al. 2013b). The spectra obtained by COBE, IRTS, and AKARI are consistent within the common wavelength region ($\lambda >$ 2 μm). Several extragalactic background light (EBL) observations were also carried out at around the optical wavelength range (Bernstein 2007; Matsuoka et al. 2011; Mattila et al. 2017a, 2017b; Kawara et al. 2017; Matsuura et al. 2017; Zemcov et al. 2017). However, their brightness levels are not in good agreement at $<0.7\,\mu$m, and this discrepancy may have been caused by uncertainties in the foreground subtraction.

The excess brightness was initially explained by the first generation of stars that formed at the reionization era (Santos et al. 2002; Salvaterra & Ferrara 2003). However, theoretical models based on the recent observations of high-redshift galaxies indicate that the first stars contribute less than 1% of the total absolute flux of the observed EBL (Cooray et al. 2012b; Yue et al. 2013). On the other hand, several studies argue that the excess brightness is not a real background but a measurement error. For example, Dwek, Krennrich, and Arendt (2005) and Kawara et al. (2017) tried to explain the excess brightness with a subtraction error of the zodiacal light (ZL) which is the brightest diffuse foreground component.

Unlike the absolute brightness measurement, the spatial fluctuation can be measured to mitigate the problem of foreground subtraction since the fluctuation is less sensitive to a foreground component. For example, although the ZL is the brightest foreground component, it is expected that ZL is very smooth over the large angular scales (Ábrahám et al. 1997; Pyo et al. 2012). Therefore, the EBL fluctuation can be more clearly distinguished from ZL. The detection of an excess EBL fluctuation was measured by Kashlinsky et al. (2005) with Spitzer at angular scales up to 5′ in wavelengths between 3.6 to 8 μm, after subtracting the contribution from galaxies brighter than mag$_{AB}$ = 25. Subsequently, an excess fluctuation was detected over the ILG at angular scales up to 1°, confirming the previous measurements (Kashlinsky et al. 2012; Cooray et al. 2012a; Mitchell-Wynne et al. 2015) using deeper and wider data from Spitzer. Using the Hubble Space Telescope data, Thompson et al. (2007) and Donnerstein (2015) measured fluctuations at 1.1 and 1.6 μm at the sub-arcminute scale. Matsumoto et al. (2011) detected excess fluctuation above 100″ from AKARI (2.4, 3.2, and 4.1 μm) data and found that the fluctuation follows a Rayleigh–Jeans like spectrum (i.e., $\lambda I_\lambda \sim \lambda^{-3}$). Using a wider-field AKARI image, Seo et al. (2015) found the existence of excess power up to $\sim$0°.3. At 1.1 and 1.6 μm, the Cosmic Infrared Background ExpeRiment (CIBER) measured large angular scale ($<1°$) fluctuations (Zemcov et al. 2014). Zemcov et al. (2014) reported a clear excess fluctuation at angular scales between 0°.1 and 0°.36. Zemcov et al. (2014) used the intra-halo light (IHL) at $z < 3$ to explain the excess fluctuation (Cooray et al. 2012a; Zemcov et al. 2014). The IHL source consists of tidally stripped stars during galaxy mergers and interactions. However, the IHL is not observationally confirmed and cannot explain all of the observed excess fluctuation. Consequently, there is no clear consensus regarding the origin of the NIREBL.

To understand the origin of the excess fluctuations, we examine the fluctuation spectrum using IRTS data with a scale up to several degrees. Such large-scale fluctuations have never been explored before. Our approach can also constrain the physical properties of the excess origins. The outline of this paper is as follows. In section 2, we introduce the instrument. We describe the observation and data reduction in section 3. The data analysis is described in section 4. The power spectrum estimation and the error estimation are shown in sections 5 and 6, respectively. The result is shown in section 7. In section 8, the discussions are given. Finally, we summarize our result in section 9.

2 Instrument

IRTS, the first Japanese orbiting IR telescope onboard the Space Flyer Unit (SFU), was launched on 1995 March

18 UT. It surveyed 7% of the sky until its liquid helium was exhausted on April 25. The IRTS is a 15 cm Ritch–Chretien type telescope with a focal length of 60 cm. The whole system, together with four focal plane instruments, was cooled down to 2 K using liquid helium (Murakami et al. 1996).

Among those instruments, the Near-Infrared Spectrometer (NIRS) is optimized to study the diffuse background with deep and wide sky coverage. The NIRS covers the wavelength range between 1.4 and 4.0 μm with a 0.13 μm spectral resolution. The incident beam goes through a 1.4 mm × 1.4 mm slit which corresponds to an 8′ × 8′ area in the sky, and it is diffracted by the grating. The dispersed beam is then focused on the linear array consisting of 24 InSb detector elements (Noda et al. 1994). To reduce the background errors arising from Galactic stars, it has a higher spatial resolution than DIRBE, and a cold shutter is installed to obtain a dark current. The stability of the detector is monitored using a calibration lamp during the observation. It uses J-FET charge integrating amplifiers operating at 60 K to detect a low background brightness by reducing the noise and achieving a high sensitivity. The InSb detector reads out data with a 4 Hz sampling rate. The charges were integrated for 65.54 s before a reset and 8.192 s of it was used for dark current observation with a shutter close configuration. Details of the NIRS performance is found in Noda et al. (1996).

3 Observation and data reduction

Of the entire IRTS coverage, we used data initially reduced by Matsumoto et al. (2005). They used data obtained at Galactic latitudes above 40° to avoid the strong foreground emissions due to the stars and dust in the Galaxy. The data obtained while passing through the South Atlantic anomaly region, where the noise level increases with high-energy charged particles, was rejected. Of the 65.54 s charge integration between resets, the first four seconds of data due to anomalous residual charges after the reset was not used. The flux (e$^-$ s^{-1}) of each IRTS data was then obtained from linear fitting of charges for five seconds along the scan direction. In the linear fitting process, contaminated data by cosmic-rays, instrumental noise, and stars were excluded. Dark current was subtracted after the linear fitting process. Details of this process are described in Matsumoto et al. (2005).

Astrometry was achieved within 2′.2 using an attitude control sensor that was accurate enough to identify the bright Galactic stars (Murakami et al. 1996). The absolute calibration was achieved with a few percent errors using the standard stars observed by the IRTS (Noda et al.

1996). The calibration factor measured from the laboratory and that derived from the observed stellar fluxes were in good agreement. The final data at 24 discrete bands covers 1% of the whole sky. From these IRTS spectra, we made the synthesized 1.6 and 2.2 μm band fluxes. Specifically, fluxes from 1.53, 1.63, and 1.73 μm were averaged to obtain the 1.6 μm flux and those from 2.03, 2.14, 2.24, and 2.34 μm were averaged to obtain the 2.2 μm flux (hereafter, IRTS SKY).

4 Data analysis

To measure the spatial fluctuation of the NIREBL, we need the brightness map of the background. The background brightness can be derived by subtracting the brightness of all astrophysical foreground components from the observed sky brightness. In this section, we describe how we estimate brightness of the observed sky and foregrounds such as diffuse Galactic light (DGL), integrated star light (ISL), and ZL.

We also performed the pixelization for the estimated brightness of each component. They were pixelized into pixels covering a nearly equal area for the power spectrum analysis since the IRTS unevenly scanned the sky. To do this, we used the well-developed tool HEALPix, which stands for the Hierarchical Equal Area isoLatitude Pixelization (Górski et al. 2005). HEALPix divides the surface of the sphere into pixels of roughly equal shape and identical size. The resolution of the pixelization is defined by $N_{\mathrm{side}} = 2^k$, where k can be any positive integer. The number of pixels in the whole sky is $12 N_{\mathrm{side}}^2$. By considering the IRTS field of view (FoV; i.e., 20′ × 8′), we used $N_{\mathrm{side}} = 64$, which corresponds to a 55′ × 55′ pixel size. This divides the whole sky into 49152 pixels.

4.1 IRTS data analysis

In this section, we describe the additional clipping process which was performed before the pixelization of the IRTS SKY. The clipping process is as follows. Using the IRTS SKY described in section 3, we did the correlation analysis with the ZL (see figure 1). Here, the estimation of the ZL is described in sub-subsection 4.2.3.

Since the ZL brightness accounts for more than 90% of the IRTS SKY, figure 1 should show a strong correlation. However, some of the IRTS data located at the low ZL brightness region does not follow the correlation. These outliers are mostly located at lower Galactic latitude regions, as shown in figure 2. This indicates that they are due to residual bright stars which were not rejected from the data reduction process. To reject these data, we fitted the correlation diagram in figure 1 linearly and excluded
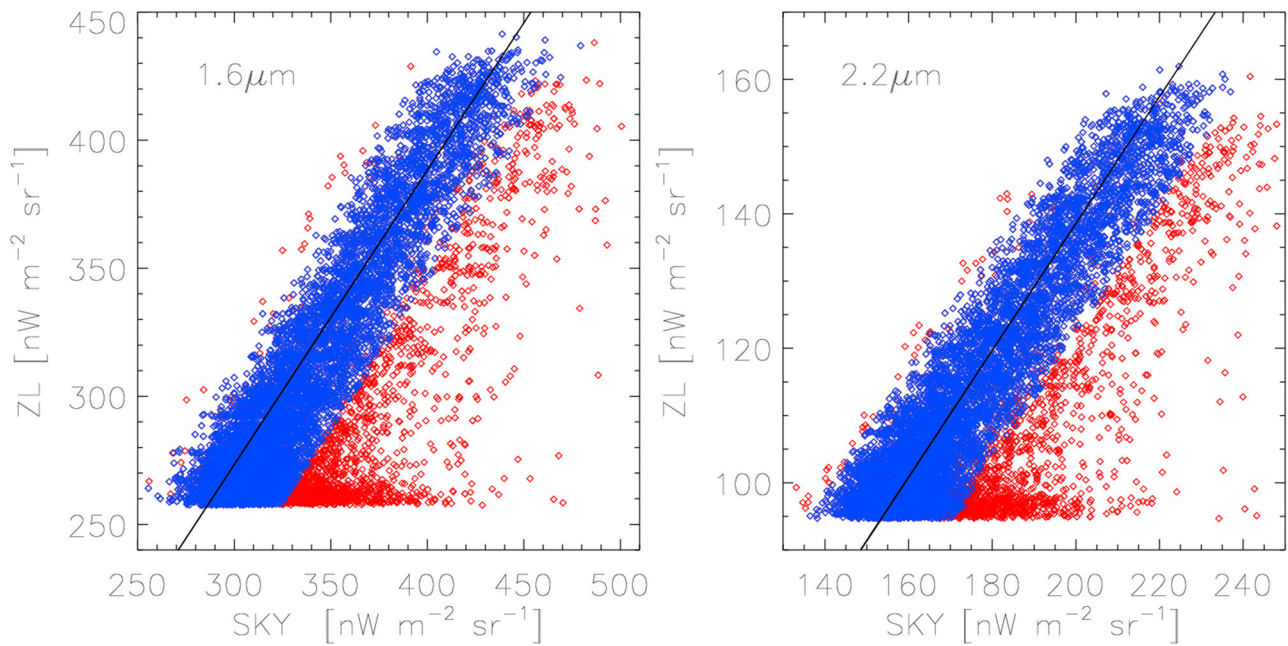
Fig. 1. Brightness correlation between the IRTS SKY and IRTS ZL. Left- and right-hand panels are 1.6 and 2.2 μm, respectively. Red symbols indicate raw data before clipping process. Blue symbols indicate data remaining after the clipping process. The black solid line is the linear fit along the most dense data regions in the raw data. (Color online)
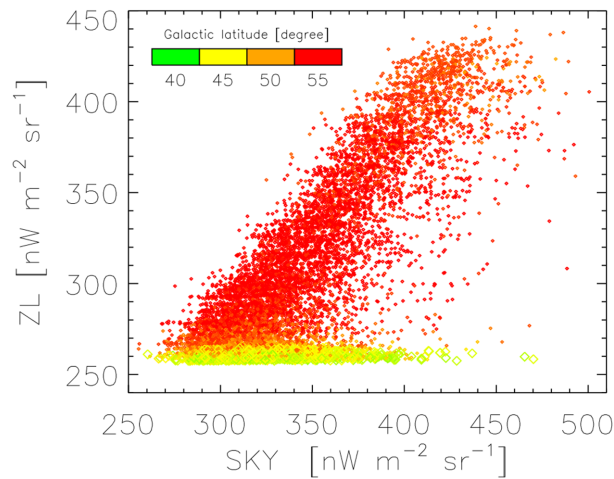

Fig. 2. Same correlation diagram as shown in figure 1 at 1.6 μm. Each data point is colored by its Galactic latitude as indicated by the color bar. To highlight the data at low Galactic latitude region ($b < 45°$), we draw them with larger symbols than others. (Color online)

Fig. 3. Number of IRTS data belonging to each HEALPix pixel. The brightness of a HEALPix pixel is the mean from the corresponding IRTS data. Here, the bin size of the histogram is 5.

the IRTS data out of 2σ which is around two times larger than the brightness range of the ISL. The fitting process was carried out as follows. On the correlation diagram in figure 1, we divided the y-axis (i.e., ZL) into constant brightness intervals. At each interval, we determined the most dense data region along the x-axis (i.e., IRTS SKY). Finally, the linear fit was carried out along those most dense data regions. Around 18% of the IRTS data was rejected through this process.
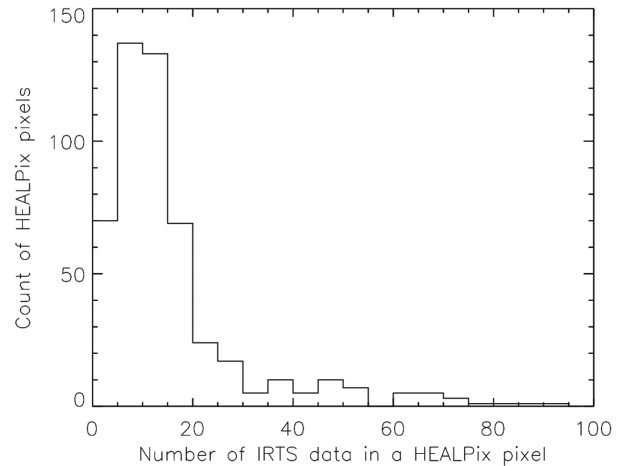
The residual IRTS data for each 1.6 and 2.2 μm was then assigned to the HEALPix pixels according to their positions. Due to the large HEALPix pixel size, a few to tens of the IRTS data belong to each HEALPix pixel. The number of IRTS data in a HEALPix pixel is shown in figure 3. The intensity of each HEALPix pixel was assigned from a mean brightness of the IRTS SKY in the HEALPix pixel. If the number of IRTS fields in a HEALPix pixel is less than 5, we masked the HEALPix pixel. 14% of the HEALPix pixels are covered by the IRTS fields. The pixelized 1.6 and 2.2 μm maps were stored in the FITS format (Calabretta & Greisen
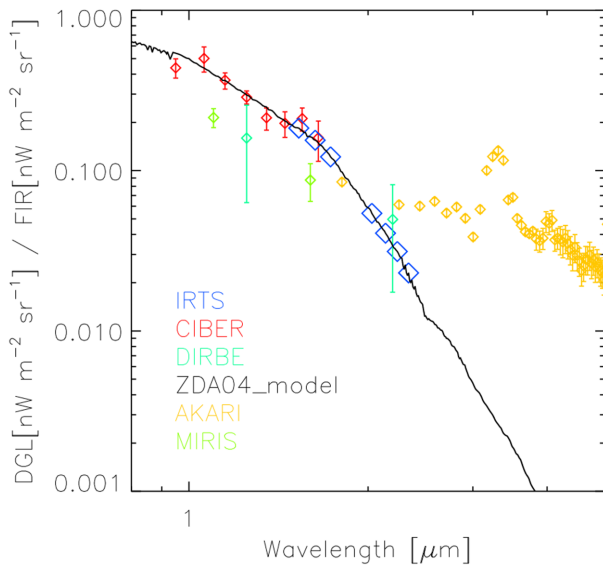
Fig. 4. DGL spectrum normalized by far-IR emission at $100\,\mu m$. The CIBER/LRS is from Arai et al. ([2015](#)), and DGL modelled to fit the CIBER/LRS data is drawn with the solid line (ZDA04; Brandt & Draine [2012](#)). Blue diamond symbols are points for the IRTS bands. The DIRBE is from Sano et al. ([2015](#)), AKARI is from Tsumura et al. ([2013a](#)), and MIRIS is from Onishi et al. ([2018](#)). Here, the AKARI data is mainly contributed by the PAH emission. Since the IRTS sky coverage is far from the Galactic plane ($b > 40°$) where contributions of PAH emission is negligible, we did not consider the AKARI data. (Color online)

[2002](#)) for the next step, to evaluate the power spectrum of the IRTS SKY.

4.2 Foreground data analysis

In this section, we describe how we estimated the foreground brightness such as DGL, ISL, and ZL. Each foreground brightness was then pixelized into a HEALPix scheme.

4.2.1 Diffuse Galactic light

The DGL consists of star light scattered from dust grains distributed in interstellar space. Since the DGL is diffuse and faint, it is difficult to observe directly. Nevertheless, far-IR thermal emission (e.g., $100\,\mu m$), H I or CO column density (Brandt & Draine [2012](#)) has a close relation with the DGL brightness. At the near-IR wavelength region, the relation between the $100\,\mu m$ thermal emission and the DGL brightness has been studied based on the near-IR observed data (Arai et al. [2015](#); Sano et al. [2015](#)). Arai et al. ([2015](#)) and Sano et al. ([2015](#)) derived a scale factor between the $100\,\mu m$ thermal emission and the near-IR DGL brightness. Then, they fitted the various model spectra to the scale factor. The best-fitted model was the Brandt and Draine ([2012](#)) model, as shown in figure [4](#). The fitted scale-factor enables us to derive the near-IR DGL brightness from the $100\,\mu m$ intensity.
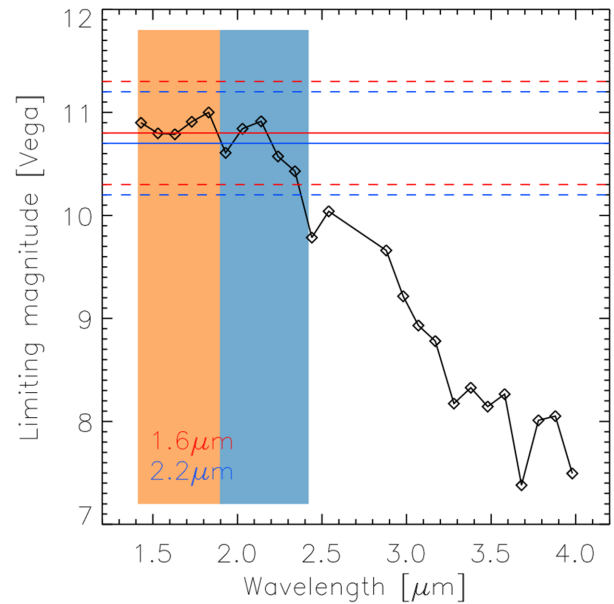

Fig. 5. Limiting magnitudes for the 24 IRTS bands (diamond symbol). Red and blue solid lines are the 1.6 and $2.2\,\mu m$ limiting magnitudes used to estimate the brightness due to unresolved Galactic stars. Also drawn in dashed lines are ± 0.5 of limiting magnitude errors. Shaded colors represent bandwidths of 1.6 and $2.2\,\mu m$. (Color online)

To estimate the DGL at IRTS fields using the scale factor as shown in figure [4](#), we used the $100\,\mu m$ thermal emission from the Schlegel, Finkbeiner, and Davis (SFD) dust map (Schlegel et al. [1998](#)). The SFD dust map was also used for the scale-factor derivation (Arai et al. [2015](#); Sano et al. [2015](#)). Nevertheless, since the SFD map was not corrected for the cosmic infrared background brightness, we subtracted $0.8\,\mathrm{MJy\,sr^{-1}}$ (Puget et al. [1996](#); Fixsen et al. [1998](#); Lagache et al. [2000](#); Matsuoka et al. [2011](#)) so the map contains only a dust emission component. From the brightness-corrected SFD map, we obtained the $100\,\mu m$ intensities belonging to each IRTS FoV. $100\,\mu m$ intensities at each IRTS FoV were then averaged. The averaged intensity was then multiplied by the scale factor at IRTS bands to derive the DGL brightness. The DGL brightness for the IRTS bands (i.e., 1.53, 1.63, 1.73, 2.03, 2.14, 2.24, and $2.34\,\mu m$) was then averaged to make synthesized DGL brightness at 1.6 and $2.2\,\mu m$ bands (hereafter, IRTS DGL). This process has been carried out for all IRTS fields and pixelized into the HEALPix scheme.

4.2.2 Integrated star light

The ISL indicates the Galactic star light which contributes to the brightness of the observed IRTS SKY. We could remove the contributions of the bright stars from the observed sky brightness. However, the contributions of faint stars could not been removed. These faint stars are defined by the limiting magnitude of the IRTS, as shown in
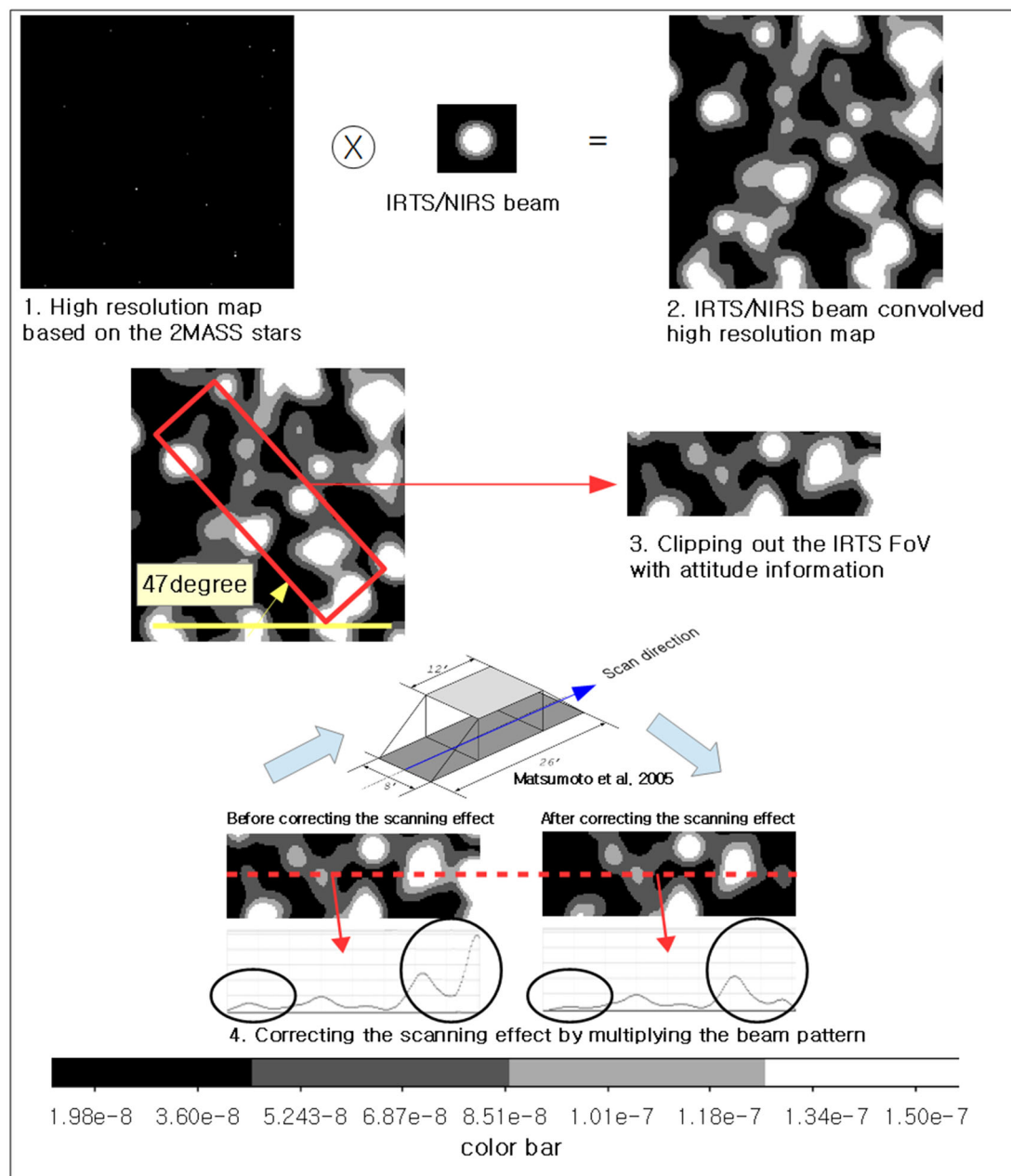
Fig. 6. Flow chart of the process to estimate the ISL brightness of an IRTS field based on the 2MASS stars. (Color online)

figure 5. In this section, we describe how we estimated the contributions of faint stars.

To estimate the ISL by faint stars above the IRTS limiting magnitude, we used a 2MASS point/extended source (Cohen et al. 2003) which is well-known Galactic star catalog in the near-IR region. Since the limiting magnitude of the 2MASS star catalog is much fainter than that of the IRTS, we could estimate the ISL caused by stars lying between the IRTS and the 2MASS limiting magnitudes. To account the faint stars even above the 2MASS limiting magnitudes, we used Galactic model stars. The 2MASS

limiting magnitudes for H and K bands are 15.1 and 14.3, respectively.

First, we describe how we estimated the ISL for IRTS fields based on the 2MASS stars. The diagram of the flow process to estimate the ISL for each IRTS field is shown in figure 6. That is, we reconstructed a high-resolution map (pixel size is 10″) where the map size is more than twice the size of the IRTS FoV. Then, we distributed the 2MASS stars on the high-resolution map where the center of the map is set by an nominal IRTS field position from the IRTS attitude information. Here, we used 2MASS stars lying between
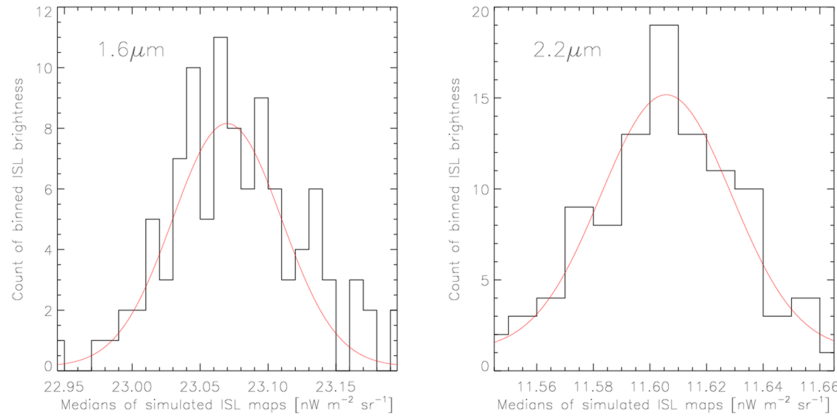
Fig. 7. Histogram of ISL medians for 100 simulated maps. Left- and right-hand panels are 1.6 and 2.2 μm, respectively. Here the bin size is 0.01 nW m^{-2} sr^{-1}. Each histogram is fitted with a Gaussian function, shown by the red solid line. (Color online)

the IRTS and the 2MASS limiting magnitudes. Then, we convolved the high-resolution map with the IRTS/NIRS beam pattern. The full width at half-maximum (FWHM) of the IRTS/NIRS beam is 2ʹ4. On the IRTS/NIRS beam convolved map, we clipped out regions covering the IRTS FoV with a center, the same as for the IRTS nominal position. However, the scanning effect during the IRTS observation causing the beam pattern is not constant along the scan direction. The effective beam pattern is trapezoidal, as shown in figure 2 of Matsumoto et al. (2005). To apply this on the clipped map, we multiplied a beam pattern which is unity at central 12ʹ region along the scan direction and linearly decreases to zero at both ends. This process has been carried out for all IRTS fields; thus the ISL based on the 2MASS stars was made.

Next, to estimate the ISL by stars above the 2MASS limiting magnitude, we used the Galactic model stars named TRILEGAL (Girardi et al. 2005). The model provides bright to faint-end stars up to limiting magnitudes of 30. It models the number of stars and their brightness in various wavelengths toward any line of sight at a specified FoV. However, since the model star does not have astrometry information, we randomly assigned the astrometry information to model stars and distributed them on the high-resolution map. Here, we used model stars fainter than the 2MASS limiting magnitude. Then, the ISL based on the model was estimated in the same manner as the ISL derivation based on the 2MASS stars. However, the brightness of the model stars is known to have a systematic offset compared with that of the 2MASS stars (see figure 1 in Matsumoto et al. 2015). To correct this, we multiplied the brightness of the ISL based on the model stars by a factor of 1.23. The ISL brightness for the 1.6 and 2.2 μm based on the model stars are 15% and 24% of the ISL brightness based on the 2MASS stars, respectively. Finally, the total ISL (hereafter, IRTS ISL) for the IRTS fields was found by

adding the ISL based on the 2MASS and the model. Then, the IRTS ISL was pixelized into the HEALPix scheme.

Here, we used the IRTS nominal position to estimate the ISL. However, the IRTS attitude information has 1σ error (i.e., 2ʹ2). This generates the brightness error on the IRTS ISL. To estimate the ISL error, we performed a simulation. That is, we reconstructed ISL maps in the same manner as shown above but using the shifted IRTS field positions within the IRTS astrometry error range. The shift amount was randomly chosen from the normal distribution having 1σ of astrometry error and added to each of the IRTS nominal positions. We repeated the simulation 100 times and made 100 ISL maps. The number of simulation (i.e., 100) was determined as follows. At each ISL map, we took the median value of brightness. We repeated the simulation until the brightness distribution of median values showed a Gaussian distribution, as shown in figure 7. Here, we used a median method as each ISL map has skewed brightness distribution towards the bright region due to bright Galactic stars. Among the simulated 100 ISL maps, we selected two maps and took brightness difference between pixels of them. Then, we calculated the 1σ from the distribution of the brightness difference. This has been done 4950 times by choosing two maps among 100 ISL maps. 4950 is the number of all possible combinations when choosing two maps among the 100 ISL maps. The 1σ values from the 4950 simulations are fairly consistent (i.e., variability relative to average is around 4%). We defined the maximum value among 4950 simulations as the ISL error, which is 1.31 nW m^{-2} sr^{-1} and 0.71 nW m^{-2} sr^{-1} for 1.6 and 2.2 μm, respectively.

4.2.3 Zodiacal light

The ZL at near-IR consists of scattered Sun light from interplanetary dust (IPD) particles in the solar system. Therefore, the ZL spectrum resembles the spectrum of the Sun.
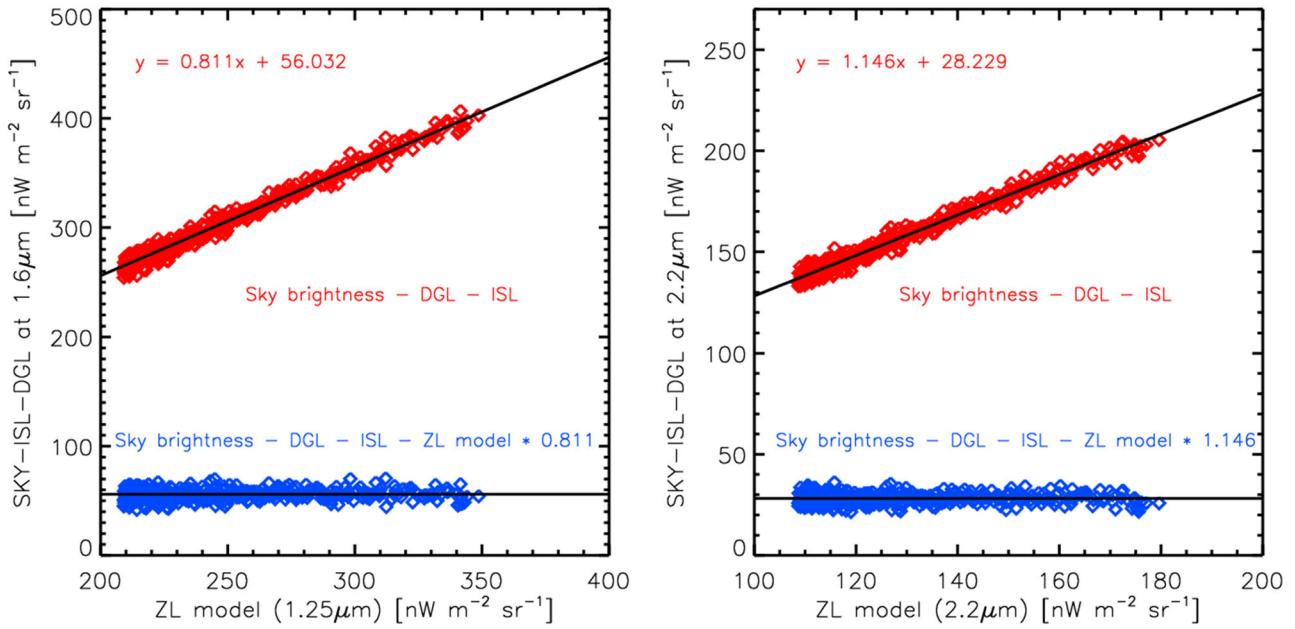
Fig. 8. Upper data points show correlation study between the ZL model brightness and the observed surface brightness after subtracting the ISL and DGL from the observed sky brightness. Lower data points are the NIREBL brightness after subtracting the corrected ZL from the *y*-axis. Black solid lines are the best-fitting lines. Left- and right-hand panels are 1.6 and 2.2 μm, respectively. (Color online)

However, the ZL brightness varies with time due to the orbital motion of the Earth around the Sun (i.e., seasonal variation). Kelsall et al. (1998) constructed a model to estimate the ZL accounting the seasonal variation. Using this model, we reconstructed the ZL map for the IRTS field. Nevertheless, we need brightness correction of the ZL model for two reasons. First, the Kelsall model does not provide the 1.6 μm ZL brightness. Therefore, we initially obtained the 1.25 μm ZL brightness and derived the 1.6 μm ZL brightness assuming that the spectral shape does not depend on the sky position (Tsumura et al. 2010). Secondly, their exists a systematic uncertainty between the ZL model and the observed ZL. The correction has been made in the same manner as Matsumoto et al. (2015). The detailed descriptions are as follows.

We obtained the 1.25 and 2.2 μm ZL model brightness (hereafter, IRTS ZL) at IRTS positions using their observation date information. Then, we pixelized the IRTS ZL into the HEALPix scheme. Next, we made brightness correlation studies between the pixelized IRTS ZL model and the IRTS data after subtracting the IRTS DGL and the IRTS ISL from the IRTS SKY. Since we subtracted the DGL and the ISL, the brightness of the IRTS data contains only brightness of the actual ZL and the NIREBL. Under the assumption that the NIREBL is homogeneous and isotropic, we expect the strong correlation with the IRTS ZL model. As shown in figure 8, there is an excellent correlation for both bands, which implies three things. First, the IRTS data after subtracting the IRTS DGL and the IRTS ISL from the IRTS SKY is well represented by the ZL. Secondly, the ZL spectral

shape is uniform for the IRTS fields. Thirdly, the NIREBL is homogeneous and has isotropic emission. According to the third implication, a slope of the correlation study should show unity. However, because of band difference and systematic uncertainty between the ZL model and actual ZL, the slopes of 1.6 and 2.2 μm are 0.811 and 1.146, respectively. The band difference and systematic uncertainty were corrected by multiplying the slopes to the ZL model brightness. Then, the IRTS ZL was pixelized into the HEALPix scheme.

5 Power spectrum analysis

In this section, we describe the power spectrum analysis of the NIREBL. The power spectrum of the NIREBL was estimated from the pixelized NIREBL brightness map. The NIREBL brightness map was derived by subtracting the IRTS DGL, IRTS ISL, and the IRTS ZL from the IRTS SKY in HEALPix format. The detailed procedure for the power spectrum analysis is described as follows.

The power spectrum is an expression of the relative brightness distributions as a function of the angular scales in degree (θ) or multipole moments (l) related by $\theta = 180/l$. The relative brightness of each map is

$$\delta I(\Theta, \Phi) = I(\Theta, \Phi) - \langle I(\Theta, \Phi) \rangle, \qquad (1)$$

where (Θ, Φ) are angular coordinates in the sky, and $\langle I(\Theta, \Phi) \rangle$ denotes the averaged brightness of the observed

region. The equation (1) can be decomposed into spherical harmonics as

$$\delta I(\Theta, \Phi) = \sum_{l=0}^{\infty} \sum_{m=-l}^{l} a_{lm} Y_{lm}(\Theta, \Phi), \qquad (2)$$

where

$$a_{lm} \sim \Omega_{\mathrm{pixel}} \sum_{i=0}^{\mathrm{Npix}} \delta I(\Theta_i, \Phi_i) Y_{lm}^*(\Theta_i, \Phi_i). \qquad (3)$$

Here, $Y_{lm}(\Theta, \Phi)$ is Laplace's spherical harmonics, a_{lm} is multipole coefficients of the expansion, and Ω_{pixel} is the solid angle of the HEAlPix pixel. $l = 0$ is a monopole and $l = 1$ is a dipole term. The power spectrum is then expressed by the variance in a_{lm} as

$$C_l = \frac{1}{2l+1} \sum_{m=-l}^{l} |a_{lm}|^2. \qquad (4)$$

However, the above procedure is only valid for the full sky coverage data with no mask. If we apply it to partial sky coverage data, it produces a biased power spectrum. Therefore, we need another approach to correct for the biases since the IRTS observed only 1% of the whole sky. There are two popular methods to measure the power spectrum for incomplete sky coverage: maximum likelihood estimation (Bond et al. 1998; Tegmark 1997) and pseudo power spectrum estimation (Hivon et al. 2002). For the IRTS power spectrum analysis, we used the publicly available PolSpice software based on the pseudo power spectrum analysis (Chon et al. 2004). Here, "pseudo" means that the isotropy assumption is broken and the PolSpice corrects for a partial sky map.

To measure the true power spectrum, PolSpice calculates a_{lm} from the $\delta I(\Theta, \Phi)$ map. Then, the pseudo power spectrum for incomplete sky coverage is calculated from equation (4). Using Legendre polynomials $P_l(\cos \eta)$, the pseudo power spectrum C_l is then converted to the correlation function

$$\xi(\eta) = \frac{1}{4\pi} \sum_{l=0}^{\infty} (2l+1) C_l P_l(\cos \eta), \qquad (5)$$

where $\xi(\eta)$ is the two-point correlation function defined by

$$\xi(\eta) = \langle \delta I(\Theta, \Phi) \delta I(\Theta', \Phi') \rangle. \qquad (6)$$

Here, the angle brackets denote the ensemble average and η is the angle between (Θ, Φ) and (Θ', Φ'). To correct for the incomplete sky coverage, the correlation function is divided by the mask correlation function, which is estimated from the mask map where the pixel value is 0 for uncovered sky

and 1 for covered sky. The corrected correlation function $\xi(\eta)$ is then inserted into the following equation to derive the true power spectrum.

$$C_l = 2\pi \int_{-1}^{1} \xi(\eta) P_l(\cos \eta) d(\cos \eta). \qquad (7)$$

As described above, the tool needs two maps in the HEALPix format. One is a brightness map and the other is a mask map that has 0 for uncovered sky and 1 for covered sky. Using the NIREBL brightness map in figure 9, we calculated the power spectrum. However, the NIREBL power spectrum still contains photon and readout noise. Since the noise level for each IRTS SKY is unknown, we performed a Monte Carlo simulation to estimate the noise power spectrum. First, we made a Gaussian distribution with a 1σ of readout noise and photon noise (Matsumoto et al. 2005). Under the Gaussian distribution assumption, we randomly picked a value for the distribution and assigned it to each IRTS field. The noise assigned map is then pixelized into the HEALPix scheme. Then, the power spectrum was estimated for the pixelized noise map. This procedure was repeated 100 times and averaged to derive the final noise power spectrum. The noise power spectrum was then subtracted from the NIREBL power spectrum for 1.6 and 2.2 μm of the IRTS.

Nevertheless, the finite resolution and pixelization can suppress the power spectrum at a small angular scale. The suppression can be corrected using a beam transfer function that depends on the shape and size of the PSF. However, we concluded that the beam transfer function for the IRTS/NIRS beam does not affect the fluctuation spectrum above $2°$, which was twice the HEALPix pixel resolution. Since the power spectrum was only valid for angular scales above $2°$ according to the Nyquist sampling, we did not apply the correction for the beam transfer function.

6 Error estimation

Errors can be categorized into random and systematic components. Random errors include sample variance of the power spectrum (i.e., $\delta I_{\mathrm{variance}}$), attitude error of the IRTS (i.e., $\delta I_{\mathrm{attitude}}$), ISL brightness error (i.e., δI_{ISL}), and binning error of the HEALPix pixel (i.e., $\delta I_{\mathrm{binning}}$). $\delta I_{\mathrm{variance}}$ is the error induced from the power spectrum estimation. At a given angular scale, the number of possible modes is limited due to a finite sky coverage. The smaller angular scale has smaller sample variance due to larger number of possible modes. However, we cannot estimate the error directly from the power spectrum analysis since the small coverage of the IRTS field results in the covariance matrix of the sample variance being very noisy. Alternatively, we used the empirically determined Knox formula that represents the
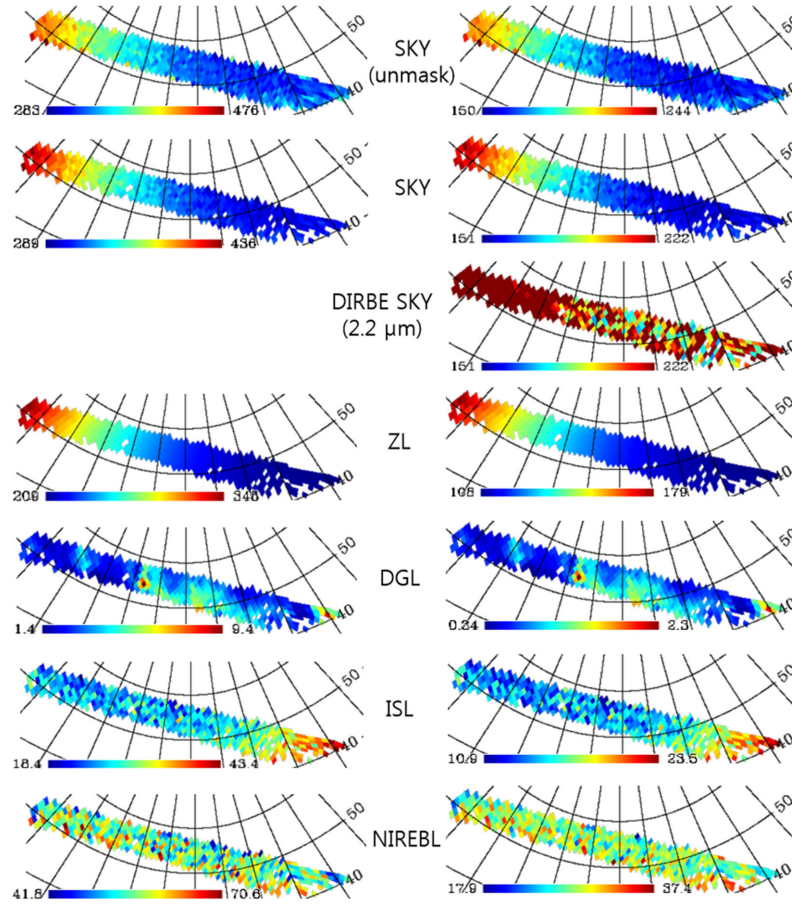
Fig. 9. Brightness maps for 1.6 and 2.2 μm in Galactic coordinates. Left- and right-hand maps are for 1.6 and 2.2 μm, respectively. Brightness maps of IRTS raw data without mask, and IRTS raw data with mask, DIRBE 2.2 μm sky map at IRTS field, ZL, DGL, ISL, and NIREBL with mask are shown from top to bottom. Units in the color bars are nW m^{-2} sr^{-1}. DIRBE 2.2 μm sky map is shown to compare with the IRTS SKY. (Color online)

χ^2 distribution of C_l with its mean (Knox 1995). The formula is given in appendix C of Thacker et al. (2015). $\delta I_{\rm ISL}$ is uncertainties of the ISL brightness. Since the uncertainties of 2MASS stars at the H and K bands are 1.95% and 1.88%, respectively, we multiplied this factor to the ISL map and take 1σ of it to derive the $\delta I_{\rm ISL}$. $\delta I_{\rm attitude}$ is the error induced from inaccurate IRTS attitude. We described the detailed procedure of $\delta I_{\rm attitude}$ calculation in sub-subsection 4.2.2. $\delta I_{\rm binning}$ is generated when computing the mean of the IRTS pixel brightness belonging to each HEALPix pixel. Our procedure to calculate $\delta I_{\rm binning}$ is as follows. First, we made a binning error map by taking 1σ of the IRTS pixel brightness belonging to each HEALPix pixel. Then, we computed 1σ of the binning error map. This procedure was carried out for each astrophysical component as well as the sky. Finally, $\delta I_{\rm binning}$ was calculated by combining all error components in a quadrature:

$$\delta I_{\rm binning} =$$

$$\sqrt{\delta I^2_{\rm SKY,binning} + \delta I^2_{\rm DGL,binning} + \delta I^2_{\rm ISL,binning} + \delta I^2_{\rm ZL,binning}} \quad (8)$$

Then, we combined all random errors using following equation excepting $\delta I_{\rm variance}$, where the power spectrum of $\delta I_{\rm variance}$ was directly calculated using the Knox formula (Knox 1995):

$$\delta I'_{\rm random} = \sqrt{\delta I^2_{\rm attitude} + \delta I^2_{\rm ISL} + \delta I^2_{\rm binning}} \quad (9)$$

The power spectrum of the $\delta I'_{\rm random}$ was calculated based on the Monte Carlo simulation in the same manner as the power spectrum calculation for the readout and photon noises described in this section. Then, the power spectrum of the total random error $\delta C_{l,\rm random}$ was calculated using equation

$$\delta C_{l,\rm random} = \sqrt{\delta C'^2_{l,\rm random} + \delta C^2_{l,\rm variance}}, \quad (10)$$

where $\delta C'_{l,\rm random}$ is the power spectrum of $\delta I'_{\rm random}$ and $\delta C_{l,\rm variance}$ is the power spectrum of $\delta I_{\rm variance}$.

The systematic errors are categorized into three. First is the calibration error of the IRTS (i.e., $\delta I_{\rm cal}$) which is known as 3% of the NIREBL brightness (Matsumoto et al. 2005, 2015). The second one is the limiting magnitude error

Table 1. Error budget for the NIREBL fluctuation.[*]

	Statistical error			Systematic error (1σ of error map)		
Band	IRTS attitude error	ISL brightness error	Healpix binning error	IRTS Calibration error	ISL limiting mag error	DGL scale-factor error
1.6 μm	1.31	0.07	0.08	0.13	1.86	0.24
2.2 μm	0.71	0.03	0.04	0.06	0.98	0.06

[*]The sample variance is not shown since it is estimated by an empirically determined Knox formula. Units are nW m^{-2} sr^{-1}.

of the IRTS (i.e., $\delta I_{\rm lim}$) where the IRTS has ± 0.5 limiting magnitude uncertainty (see figure 5). Third is the model error of the DGL (i.e., $\delta I_{\rm DGL}$). Here, we did not consider the error of the ZL model (Kelsall et al. 1998) since the error does not affect the fluctuation analysis, only the absolute brightness analysis. The $\delta I_{\rm cal}$ was computed by multiplying the NIREBL brightness map by 0.03. $\delta I_{\rm lim}$ causes the systematic brightness difference on the ISL. To compute this, we derived the ISL brightness error (i.e., $\delta I'_{\rm lim}$) after adding ± 0.5 to the limiting magnitude of the IRTS. The $\delta I'_{\rm lim}$ derivation was the same as the nominal ISL brightness (i.e., $\delta I_{\rm nominal}$) derivation described in sub-subsection 4.2.2. Then, we took the brightness difference between $\delta I'_{\rm lim}$ and $\delta I_{\rm nominal}$. We set the difference as the ISL error (i.e., $\delta I_{\rm lim}$) caused by the error of the IRTS limiting magnitude. $\delta I_{\rm DGL}$ is transferred from the scale factor which is needed to convert 100 μm intensity (i.e., far-IR) to near-IR DGL brightness as described in sub-subsection 4.2.1. Arai et al. (2015) compared the DGL model to the observed data and found that the scale factor has 20% uncertainty. To account for this error, we multiplied the DGL brightness map by 0.2 and derived the error amount of DGL brightness $\delta I_{\rm DGL}$. The power spectrum of each error component is calculated based on the Monte Carlo simulation in the same manner as $\delta C_{l,\rm random}$. Then, the power spectrum of the total systematic error is calculated using the equation

$$\delta C_{l,\rm systematic} = \delta C_{l,\rm calibration} + \delta C_{l,\rm lim} + \delta C_{l,\rm DGL}. \quad (11)$$

Finally, the power spectrum of total error was calculated using

$$\delta C_{l,\rm total} = \sqrt{\delta C_{l,\rm random}^2 + \delta C_{l,\rm systematic}^2}. \quad (12)$$

The brightness of errors listed above, excepting $\delta I_{\rm variance}$, are shown in table 1.

7 Result

The fluctuation spectra of the NIREBL for 1.6 and 2.2 μm are shown in figures 10 and 11, respectively. In figure 10, the IRTS fluctuation shows a power law with an angular scale.
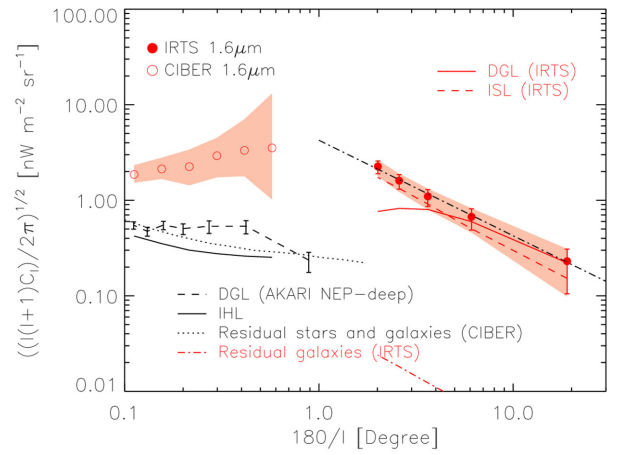

Fig. 10. Measured 1.6 μm fluctuations for the IRTS. The IRTS (this work) and the CIBER (Zemcov et al. 2014) auto spectra are shown by the filled and unfilled red circles, respectively. The shaded color of the IRTS shows the error including systematic error and the random error is drawn with an error bar. The shaded color for the CIBER denotes estimated errors. The black dot–dashed line is a power law with index -1. Solid and dashed lines in red are DGL and ISL for IRTS, respectively. The red dot–dashed line is spectrum due to unresolved galaxies. The dashed line is the DGL spectrum measured using the AKARI/FIS deep pointing data toward NEP region (Seo et al. 2015). Dotted and solid lines are unmasked sources (i.e., stars and galaxies for $m_H > 17$) and IHL spectrum from Zemcov et al. (2014), respectively. (Color online)

The power index close to -1 indicates that the fluctuation is random and structureless. This homogeneous and isotropic feature is also shown in the NIREBL map in figure 9. For comparison, the fluctuation spectrum of the CIBER project (Zemcov et al. 2014) at a smaller angular scale ($<1°$) is also shown. There seems to be a smooth connection between the IRTS and the CIBER. Although there exists no data between them, we can infer that the NIREBL fluctuation has a peak at around 1°.

In figure 11, we also examined the fluctuation at the 2.2 μm. Since the CIBER does not have 2.2 μm data, we needed to multiply a scale factor to the CIBER 1.6 μm power spectrum. The scale factor was derived by the IRTS 1.6/2.2 μm color ratio, assuming the color of the NIREBL does not depend on the sky position. The ratio was derived from the IRTS 1.6 and 2.2 μm correlation study as shown in figure 12. Then the ratio was multiplied to the CIBER
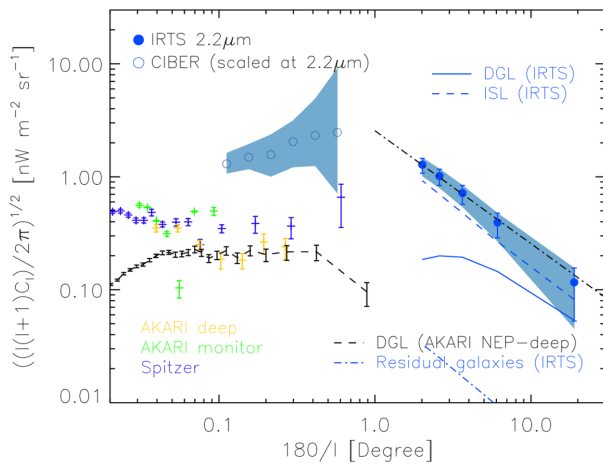
Fig. 11. The measured 2.2 μm fluctuations for the IRTS. The IRTS (this work) and the CIBER (Zemcov et al. 2014) auto spectra are shown by the filled and unfilled blue circles, respectively. The shaded color of the IRTS shows the error including systematic error and the random error is drawn with an error bar. The shaded color for the CIBER denotes estimated errors. The black dot–dashed line is a power law with index -1. Solid and dashed lines in red are DGL and ISL for IRTS, respectively. The blue dot–dashed line is the spectrum due to unresolved galaxies. The CIBER 1.6 μm is scaled to 2.2 μm using IRTS 1.6/2.2 μm color ratio. Plus signs with errors are the fluctuation spectra from the AKARI 2.4 μm (Matsumoto et al. 2011; Seo et al. 2015) and Spitzer 3.6 μm (Kashlinsky et al. 2012). Their spectra are scaled to 2.2 μm under the Rayleigh–Jeans assumption. The dashed line is the DGL spectrum measured using the AKARI/FIS deep pointing data toward NEP region (Seo et al. 2015). (Color online)
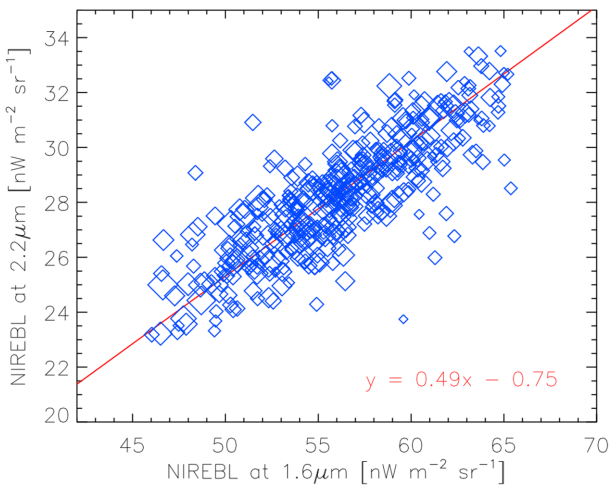

Fig. 12. The correlation between the 1.6 and 2.2 μm NIREBL brightness after subtraction of the astrophysical foreground components from the IRTS data. Each data point has a different symbol size inversely weighted by its error. That is, the larger symbol represents the smaller error. The best linear fit is shown in red solid line. The fitting parameters are shown in the bottom right-hand corner of the figure. (Color online)

1.6 μm power spectrum to derive the CIBER 2.2 μm one. As well as the CIBER, we also compared fluctuation spectra for AKARI 2.4 μm (Matsumoto et al. 2011; Seo et al. 2015) and Spitzer 3.6 μm (Kashlinsky et al. 2012) by scaling the

amplitude of their fluctuations to the 2.2 μm under the Rayleigh–Jeans assumption (Matsumoto et al. 2011).

As a result, the fluctuation spectra from AKARI and Spitzer are marginally consistent with each other. Especially, the Spitzer data are extended toward larger angular scales where the fluctuation amplitude is 10 times larger than that of the ILG. The discrepancy between the CIBER and the other measurements (i.e., Spitzer and AKARI) may indicate that the contributing components of the NIREBL are somehow different depending on the wavelengths. Otherwise, since the scaling is only valid if fluctuation follows a Rayleigh–Jeans like spectrum, the discrepancy may occur as a result of the scale factors. Nevertheless, their similar spectral shapes indicate they have same origin. Furthermore, the fluctuation spectrum of the IRTS at 2° is located at the middle of the CIBER and the Spitzer fluctuations, so either case implies a peak at around 1° angular scale. Evidently, the 1° peak seems to be a common feature in the broad wavelength ranges in the near-IR.

We also examined the IRTS 1.6 and 2.2 μm brightness correlation. As shown in figure 12, the 1.6 and 2.2 μm show excellent correlations. The 1.6/2.2 μm ratio is consistent with that from the NIREBL brightness spectrum obtained by Matsumoto et al. (2015). In addition, we derived the absolute brightness of the NIREBL using results shown in figure 8. The y-intercept, where the brightness of the ZL becomes zero, represents the absolute brightness of the NIREBL; they are 56.032 and 28.228 nW m^{-2} sr^{-1} for the 1.6 and 2.2 μm, respectively. They are fairly consistent with those of Matsumoto et al. (2015), which implies that our NIREBL brightness derivation is reasonable. This confirms consistency in the data analysis, and the excess fluctuation is strongly associated with the NIREBL spectrum.

8 Discussion

To find the possible origin of excess power at around 1°, we examined several candidate sources. High-redshift objects (e.g., first stars) were initially excluded since they show a turnover at around 0°3, which contradicts with the peak fluctuation at around 1° (see figure A-2 in Kashlinsky et al. 2012).

The first candidate is the foreground, such as ISL, DGL, or ZL. To check this, we analyzed the cross-correlation between each foreground component and NIREBL using the PolSpice analysis tool. However, none of the foreground components show correlation with the NIREBL. As a reference, the ISL and the DGL fluctuations are shown in figures 10 and 11. Since the ZL is based only on the model, we do not evaluate the ZL fluctuation in this work. According to Zemcov et al. (2014), however, the ZL fluctuation is too small to detect the fluctuation power.

The second candidate is the IHL. The IHL fluctuation can be composed of one- and two-halo terms (Cooray et al. 2012a). The one-halo term describes the clustering of baryonic matter inside a halo, and the two-halo term describes the correlations between the individual halos. The two-halo term shows larger power fluctuation than the one-halo term. In figure 10, we draw the contribution of the IHL from Zemcov et al. (2014) and compare it to the NIREBL fluctuations. Although the IHL spectrum was only estimated at sub-degree scales, the amplitude was too low to explain the excess at $1°$.

Next is the DGL, which accounts for a large portion of the fluctuation at a small angular scale measurement (Zemcov et al. 2014). Gautier et al. (1992) empirically derived that the DGL power spectrum (C_l) follows l^{-3} of a power-law. If we extend the DGL spectrum at Zemcov et al. (2014) towards a larger angular scale with a constant power-law, the excess emission of the IRTS can be explained. However, their DGL estimation was obtained from a low angular resolution map (Schlegel et al. 1998) and we may expect a slower increase than θ^3 towards larger angular scales.

To measure the DGL directly without a power-law extrapolation at sub-degree scales, we used a high-resolution (pixel scale $\sim 0\!\!.\!16$) and a deep pointing AKARI $90\,\mu m$ image of the North Ecliptic Pole (NEP) region (Seo et al. 2015). The intensity of the map was scaled to near-IR using the empirical scaling relation in the same manner as described in sub-subsection 4.2.1. We then measured the power spectrum using POKER which is a publicly available tool.[1] POKER estimates the power spectrum using a Fourier transform under the flat sky approximation. Since projecting the observed sky on to a plane distorts the data, it is only applicable for an image of less than a few degrees (Ponthieu et al. 2011). The flat-sky approximation is valid for the AKARI image with a FoV of $1\!\!.\!2 \times 1\!\!.\!2$.

The estimated DGL fluctuation is consistent with the CIBER at smaller angular scales but decreases toward larger angular scales, as shown in figures 10 and 11. Although the DGL intensity depends on the field position, the overall shape of the DGL fluctuation at the degree scale also decreases, as shown in figures 10 and 11. Furthermore, the cross-correlation between the DGL and the NIREBL indicates that the DGL does not contribute to the NIREBL.

We examined the possibility of stellar contamination on the residual background, which can be imperfectly subtracted. If the NIREBL has residual stellar contribution, the $1.6/2.2\,\mu m$ ratios of the NIREBL and that of the stars are similar. To check this, we derived $1.6/2.2\,\mu m$ ratio of 2MASS stars in the IRTS fields. The derived ratio is 0.57,

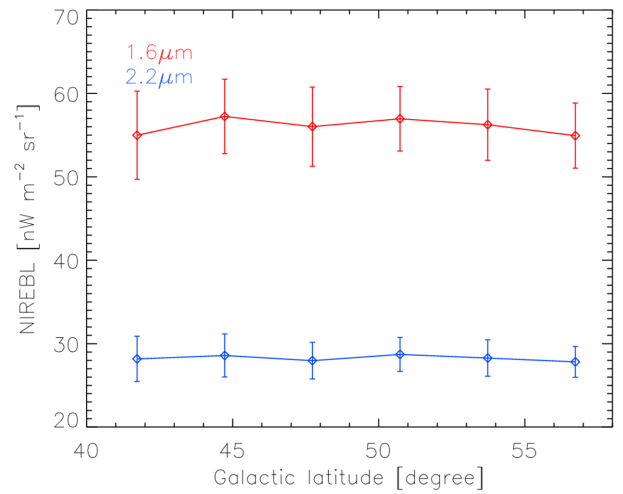**Fig. 13.** NIREBL brightness dependence along the Galactic latitude bin. Here the bin size is $3°$. The 1σ error of each bin is drawn. The upper and lower curves are for 1.6 and $2.2\,\mu m$, respectively. (Color online)

which is only 15% steeper than the $1.6/2.2\,\mu m$ ratio of the NIREBL in figure 12. Since the difference is not significant, we additionally checked whether a Galactic latitude dependency exists on the NIREBL map, as shown in figure 13. Here, we average the brightness of the NIREBL map with a constant interval (i.e., $3°$) of the Galactic latitude. Nevertheless, it shows no dependency along the Galactic latitude, which indicates that the Galactic stars are not proper candidates.

We compared the IRTS with the DIRBE (see figure 9 for DIRBE map). Since the DIRBE has much brighter detection limit (i.e., $\sim 3\,mag$), stellar contribution is mainly due to nearby bright stars and thus no Galactic latitude dependency is shown. However, they carefully subtracted the Galactic stars to achieve an homogeneous background map. Using a much more sensitive IRTS image but poor attitude information, the 1σ of the NIREBL brightness distribution at $2.2\,\mu m$ is $2.16\,nW\,m^{-2}\,sr^{-1}$, which is fairly consistent with the DIRBE $2.2\,\mu m$ study (Levenson et al. 2007).

A fraction of the NIREBL brightness is also contributed by normal galaxies. To estimate the contribution of the galaxy at the degree scale, we performed Monte Carlo simulations using the galaxy count model presented by Keenan et al. (2010). We made a brightness map by randomly distributing the galaxies in the sky based on the model count and calculated the power spectrum. We then repeated this procedure 10 times and made 10 maps. We calculated the power spectrum of each map and took average of those power spectra. Nevertheless, they contribute less than 1% of the NIREBL fluctuation level for 1.6 and $2.2\,\mu m$ at large angular scales (see figures 10 and 11).

We also examined the near-IR and far-IR cross-correlation using the PolSpice analysis tool. For the near-IR

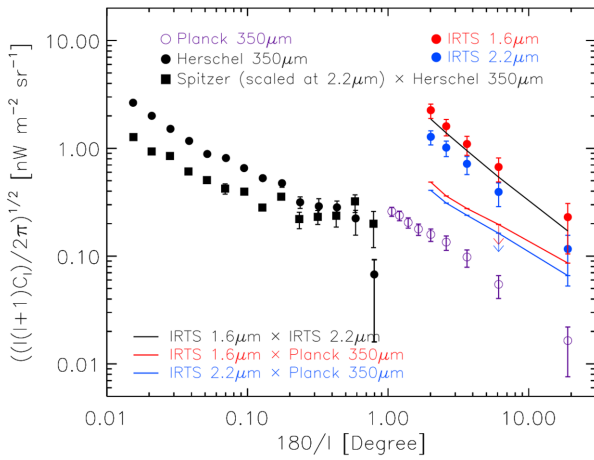[1] ⟨http://www.ipag.osug.fr/~ponthien/Poker/Poker.html⟩.

Fig. 14. Auto-correlation fluctuation spectra of Herschel 350 μm (Thacker et al. 2015) and Planck 350 μm (this work), together with cross-correlations of Spitzer 3.6 μm and Herschel 350 μm (Thacker et al. 2015), IRTS 1.6 μm and Planck 350 μm (this work), and IRTS 2.2 μm and Planck 350 μm (this work). Auto-correlation fluctuation spectra of IRTS 1.6 μm and 2.2 μm (this work) are also drawn. Only upper limits (arrows with solid lines) of cross-correlation between the IRTS bands and Planck are shown because of large errors. The Spitzer spectrum is scaled to 2.2 μm under the Rayleigh–Jeans assumption. (Color online)

map, we used the NIREBL map reduced from this work. For the far-IR map, we used the cosmic infrared background (CIB) map reduced from the Planck 857 GHz data. The Planck team provides a Galactic thermal dust and cosmic microwave background (CMB) removed Planck map[2] where the residual brightness contains only the extragalactic CIB component. According to Planck Collaboration (2011), the Planck map is composed of dusty, star-forming galaxies mostly from a low redshift ($z < 0.8$). The auto-correlation spectrum for Planck is shown in figure 14. The fluctuation seems to have a smooth connection with the Herschel 350 μm one (Thacker et al. 2015) towards smaller angular scales.

Interestingly, the IRTS and the Planck show a good correlation, although only the upper bound is shown due to a large error (see figure 14). If the nominal cross-spectrum is near the upper bound, the fluctuation spectrum (i.e., cross correlation between the IRTS K and the Planck) smoothly connects with the Spitzer (3.6 μm) spectrum crossing the Herschel (350 μm) spectrum (Thacker et al. 2015), with a peak at around 1° on the angular scale. Note that the Spitzer (3.6 μm) spectrum is scaled to the IRTS 2.2 μm under the Rayleigh–Jeans assumption for the comparison. According to the measurements at the sub-degree scale by Thacker et al. (2015), about half of the near-IR background can be explained by dusty, star-forming galaxies, and the residuals can be explained by the IHL. However, it is difficult

2 ⟨http://pla.esac.esa.int/pla⟩.

to explain the whole excess at degree scales since only the upper limits were obtained.

Since the sources contributing to the fluctuations of the near-IR background at such large angular scales have not been clearly identified, we examined possible candidates. However, none of them seem to show a significant contribution. Thus, future studies are necessary to understand the anisotropies from sub-degree to degree scales.

9 Summary

We measure the NIREBL fluctuation spectra at angular scales between 2° to 20° for the 1.6 and 2.2 μm for the first time. The NIREBL power spectrum is calculated from the NIREBL brightness map after subtracting the foreground components, such as the DGL, the ISL, and the ZL, from the observed sky brightness. The readout and photon noises of the IRTS are subtracted from the power spectrum. Within the range of the angular scale studied here, the NIREBL fluctuation monotonically declines with a $F[\sqrt{l(l+1)C_l/2\pi}] \sim \theta^{-1}$ constant power-law, indicating that the fluctuations at an angular scale greater than 2° are random and structureless. The bumpy structures in Matsumoto et al. (2005) are also reduced in this work by correcting the effect of the mask pixels on the power spectrum. Furthermore, compared with Matsumoto et al. (2005), our study achieves larger sky coverage and thus larger two-dimensional sampling, which enables us to compare fluctuations with other studies directly. Our results are also consistent with Matsumoto et al. (2015) for the 1.6 and 2.2 μm absolute brightness measurement. This implies that the sky fluctuation is strongly related to the NIREBL spectrum. Comparing the results with previous studies at sub-degree scales, both the 1.6 and 2.2 μm spectra appear to have broad bumps with a center at around 1°. We examine several proposed origins explaining the sub-degree scale fluctuations, but these are not likely to contribute to the fluctuations at degree scales. Interestingly, the fluctuations at 857 GHz with Planck after the subtraction of the foreground and CMB suggest a good correlation with those of the IRTS bands, although we can only set the upper limit, due to large uncertainties. If they have a significant correlation, this indicates that some portions of the anisotropies at degree scales can be explained by dusty, star-forming galaxies at $z < 0.8$. Recently, the Korean space mission MIRIS performed deep observations towards the large area near the NEP region (10° × 10°). The data is being processed and is expected to probe the fluctuations in the spectrum at around 1° to several-degree scales. This work provides motivation to study various kinds of background that can contribute to the degree-scale fluctuations.

Acknowledgments

References

Ábrahám, P., Leinert, C., & Lemke, D. 1997, A&A, 328, 702

Arai, T., et al. 2015, ApJ, 806, 69

Bernstein, R. A. 2007, ApJ, 666, 663

Bond, J. R., Jaffe, A. H., & Knox, L. 1998, Phys. Rev. D, 57, 2117

Brandt, T. D., & Draine, B. T. 2012, ApJ, 744, 129

Calabretta, M. R., & Greisen, E. W. 2002, A&A, 395, 1077

Cambrésy, L., Reach, W. T., Beichman, C. A., & Jarrett, T. H. 2001, ApJ, 555, 563

Chon, G., Challinor, A., Prunet, S., Hivon, E., & Szapudi, I. 2004, MNRAS, 350, 914

Cohen, M., Wheaton, Wm. A., & Megeath, S. T. 2003, AJ, 126, 1090

Cooray, A., et al. 2012a, Natur, 490, 514

Cooray, A., Gong, Y., Smidt, J., & Santos, M. G. 2012b, ApJ, 756, 92

Donnerstein, R. L. 2015, MNRAS, 449, 1291

Dwek, E., Krennrich, F., & Arendt, R. 2005, ApJ, 634, 155

Fixsen, D. J., Dwek, E., Mather, J. C., Bennett, C. L., & Shafer, R. A. 1998, ApJ, 508, 123

Gautier, T. N., III, Boulanger, F., Perault, M., & Puget, J. L. 1992, AJ, 103, 1313

Girardi, L., Groenewegen, M. A. T., Hatziminaoglou, E., & da Costa, L. 2005, A&A, 436, 895

Gorjian, V., Wright, E. L., & Chary, R. R. 2000, ApJ, 536, 550

Górski, K. M., Hivon, E., Banday, A. J., Wandelt, B. D., Hansen, F. K., Reinecke, M., & Bartelmann, M. 2005, ApJ, 622, 759

Hivon, E., Górski, K. M., Netterfield, C. B., Netterfield, C. B., Crill, B. P., Prunet, S., & Hansen, F. 2002, ApJ, 567, 2

Kashlinsky, A., Arendt, R. G., Ashby, M. L. N., Fazio, G. G., Mather, J., & Moseley, S. H. 2012, ApJ, 753, 63

Kashlinsky, A., Arendt, R. G., Mather, J., & Moseley, S. H. 2005, Nature, 438, 45

Kawara, K., Matsuoka, Y., Sano, K., Brandt, T. D., Sameshima, H., Tsumura, K., Oyabu, S., & Ienaka, N. 2017, PASJ, 69, 31

Keenan, R. C., Barger, A. J., Cowie, L. L., & Wang, W.-H. 2010, ApJ, 723, 40

Kelsall, T., et al. 1998, ApJ, 508, 44

Knox, L. 1995, Phys. Rev. D, 52, 4307

Lagache, G., Haffner, L. M., Reynolds, R. J., & Tufte, S. L. 2000, A&A, 354, 247

Levenson, L. R., Wright, E. L., & Johnson, B. D. 2007, ApJ, 666, 34

Matsumoto, T., et al. 2005, ApJ, 626, 31

Matsumoto, T., et al. 2011, ApJ, 742, 124

Matsumoto, T., Kim, M. G., Pyo, J., & Tsumura, K. 2015, ApJ, 807, 57

Matsuoka, Y., Ienaka, N., Kawara, K., & Oyabu, S. 2011, ApJ, 736, 119

Matsuura, S., et al. 2017, ApJ, 839, 7

Mattila, K., Lehtinen, K., Väisänen, P., von Appen-Schnur, G., & Leinert, Ch. 2017a, MNRAS, 470, 2133

Mattila, K., Väisänen, P., Lehtinen, K., von Appen-Schnur, G., & Leinert, Ch. 2017b, MNRAS, 470, 2152

Mitchell-Wynne, K., et al. 2015, Nature Comm., 6, 7945

Murakami, H., et al. 1996, PASJ, 48, L41

Noda, M., Matsumoto, T., Matsuura, S., Noguchi, K., Tanaka, M., Lim, M. A., & Murakami, H. 1994, ApJ, 428, 363

Noda, M., Matsumoto, T., Murakami, H., Kawada, M., Tanaka, M., Matsuura, S., & Guo, H. 1996, Proc. SPIE, 2817, 248

Onishi, Y., et al. 2018, PASJ, 70, 76

Planck Collaboration 2011, A&A, 536, A18

Ponthieu, N., Grain, J., & Lagache, G. 2011, A&A, 535, 90

Puget, J.-L., Aberget, A., Bernard, J.-P., Boulanger, F., Burton, W. B., Desert, F.-X., & Hartmann, D. 1996, A&A, 308, L5

Pyo, J., Matsumoto, T., Jeong, W.-S., & Matsuura, S. 2012, ApJ, 760, 102

Salvaterra, R., & Ferrara, A. 2003, MNRAS, 339, 973

Sano, K., Kawara, K., Matsuura, S., Kataza, H., Arai, T., & Matsuoka, Y. 2015, ApJ, 811, 77

Sano, K., Kawara, K., Matsuura, S., Kataza, H., Arai, T., & Matsuoka, Y. 2016, ApJ, 818, 72

Santos, M. R., Bromm, V., & Kamionkowski, M. 2002, MNRAS, 336, 1082

Schlegel, D. J., Finkbeiner, D. P., & Davis, M. 1998, ApJ, 500, 525

Seo, H. J., Lee, H. M., Matsumoto, T., Jeong, W.-S., Lee, M. G., & Pyo, J. 2015, ApJ, 807, 140

Tegmark, M. 1997, Phys. Rev. D, 55, 5895

Thacker, C., Gong, Y., Cooray, A., De Bernardis, F., Smidt, J., & Mitchell-Wynne, K. 2015, ApJ, 811, 125

Thompson, R. I., Eisenstein, D., Fan, X., Rieke, M., & Kennicutt, R. C. 2007, ApJ, 666, 658

Tsumura, K., et al. 2010, ApJ, 719, 394

Tsumura, K., Matsumoto, T., Matsuura, S., Sakon, I., Tanaka, M., & Wada, T. 2013a, PASJ, 65, 120

Tsumura, K., Matsumoto, T., Matsuura, S., Sakon, I., & Wada, T. 2013b, PASJ, 65, 121

Wright, E. L., & Reese, E. D. 2000, ApJ, 545, 43

Yue, B., Ferrara, A., Salvaterra, R., & Chen, X. 2013, MNRAS, 431, 383

Zemcov, M., et al. 2014, Science, 346, 732

Zemcov, M., et al. 2017, Nature Comm., 8, 15003